

This is an Open Access document downloaded from ORCA, Cardiff University's institutional repository: <https://orca.cardiff.ac.uk/id/eprint/136914/>

This is the author's version of a work that was submitted to / accepted for publication.

Citation for final published version:

Chraiki, Ibtissam, Bouougri, El Hafid, Chi Fru, Ernest, Lazreq, Nezha, Youbi, Nasrddine, Boumehdi, Ahmed, Aubineau, Jérémie, Fontaine, Claude and El Albani, Abderrazak 2021. A 571 million-year-old alkaline volcanic lake photosynthesizing microbial community, the Anti-atlas, Morocco. *Geobiology* 19 (2), pp. 105-124. 10.1111/gbi.12425

Publishers page: <http://dx.doi.org/10.1111/gbi.12425>

Please note:

Changes made as a result of publishing processes such as copy-editing, formatting and page numbers may not be reflected in this version. For the definitive version of this publication, please refer to the published source. You are advised to consult the publisher's version if you wish to cite this paper.

This version is being made available in accordance with publisher policies. See <http://orca.cf.ac.uk/policies.html> for usage policies. Copyright and moral rights for publications made available in ORCA are retained by the copyright holders.



**Ibtissam Chraiki<sup>1</sup>, El Hafid Bouougri<sup>1</sup>, Ernest Chi Fru<sup>2</sup>, Nezha Lazreq<sup>1</sup>,  
Nasrddine Youbi<sup>1,3,4</sup>, Ahmed Boumehdi<sup>1,3</sup>, Jérémie Aubineau<sup>5</sup>, Claude Fontaine<sup>5</sup>,  
Abderrazak El Albani<sup>5</sup>**

<sup>1</sup>Department of Geology, Faculty of Sciences-Semlalia, Cadi Ayyad University, Marrakesh,  
Morocco.

<sup>2</sup>College of Physical and Engineering Sciences, School of Earth and Ocean Sciences, Centre  
for Geobiology and Geochemistry, Cardiff University, Cardiff CF10 3AT, Wales, UK

<sup>3</sup>Instituto Dom Luiz, University of Lisbon, Portugal.

<sup>4</sup>Faculty of Geology and Geography, Tomsk State University, Tomsk, Russia

<sup>5</sup>University of Poitiers, CNRS IC2MP UMR 7285, Poitiers, France.

## **Correspondence**

Abderrazak El Albani,  
University of Poitiers, CNRS IC2MP UMR 7285, Poitiers, France  
Email: [abder.albani@univ-poitiers.fr](mailto:abder.albani@univ-poitiers.fr)



## Abstract

The Ediacaran period coincides with the emergence of ancestral animal lineages and cyanobacteria capable of thriving in nutrient deficient oceans which together with photosynthetic eukaryotic dominance, culminated in the rapid oxygenation of the Ediacaran atmosphere. However, ecological evidence for the colonization of the Ediacaran terrestrial biosphere by photosynthetic communities and their contribution to the oxygenation of the biosphere at this time is very sparse. Here, we expand the repertoire of Ediacaran habitable environments to a specific microbial community that thrived in an extreme alkaline volcanic lake 571 Myr ago in the Anti-atlas of Morocco. The microbial fabrics preserve evidence of primary growth structures, comprised of two main microbialitic units, with the lower section consisting of irregular and patchy thrombolitic mesoclots associated with composite microbialitic domes. Calcirudite interbeds, dominated by wave-rippled sandy calcarenites and stromatoclasts, fill the interdome troughs and seal the dome tops. A meter-thick epiclastic stromatolite bed grading upwards from a dominantly flat to wavy laminated base, transitions into low convex laminae consisting of decimeter to meter-thick dome-shaped stromatolitic columns, overlies the thrombolitic and composite microbialitic facies. Microbialitic beds constructed during periods of limited clastic input, and underlain by coarse-grained microbialite-derived clasts and by the wave-rippled calcarenites, suggest high-energy events associated with lake expansion. High-resolution microscopy revealed spherulitic aggregates and structures reminiscent of coccoidal microbial cell casts and mineralized extra-polymeric substances (EPS). The primary fabrics and multistage diagenetic features represented by active carbonate production, photosynthesizing microbial communities, photosynthetic gas bubbles, gas-escape structures, and tufted mats, suggest specialized oxygenic photosynthesizers thriving in alkaline volcanic lakes, contributed towards oxygen variability in the Ediacaran terrestrial biosphere.

48

49    **Keywords:** stromatolites; thrombolites; lacustrine, Ediacaran, oxygen; oxygenation

50

## Introduction

Microbialites are lithified bio-sedimentary deposits formed through the trapping and binding of sediment grains by benthic microbial communities and/or in situ mineral precipitation and organomineralisation (Eymard, Alvarez, Bilmes, Vasconcelos, & Ariztegui 2020; Riding, 1991). These biologically derived organo-sedimentary structures vary in shape, including columnar, sheet-like and domal structures, dependent upon the microbial community involved in their construction, the environment, physicochemical conditions, and the level of overlay.

Microbial deposits can be laminated or non-laminated, based on their framework. For example, stromatolites form laminated microbial deposits, while thrombolites, dendrolites and leiolites represent non-laminated microbialites, all displaying diverse shapes and fabrics (Noffke & Awramik, 2013; Riding, 2011). Laminated and lithified microbial deposits may preserve a variety of fine- and coarse-grained fabrics (Riding, 2011; Suarez-Gonzalez, Benito, Quijada, Mas, & Campos-Soto 2019). Fine-grained carbonate microbialites consist usually of alternating micrite and microsparite laminae that occasionally preserve calcified microbes that show up mainly as products of syngenetic microbial precipitation. Clotted and peloidal fine-grained microfabrics are broadly similar to those produced by heterotrophic bacterial calcification of EPS and other cell products.

Moreover, it is widely accepted that cyanobacteria, together with whole community metabolic activity, are crucial to sedimentary carbonate production by precipitating and incorporating carbonate into the protective sheaths and EPS (Dupraz & Visscher, 2005; Altermann et al., 2006). Interactions between heterotrophic microorganisms and cyanobacteria communities are believed to have contributed significantly to carbonate biomineralization as far back as the late Archean (Bosak, Knoll, & Petroff 2013). The trapping of sand particles by uncalcified EPS and microbial filaments, including those produced by microalgae, construct coarse agglutinated

stromatolitic and thrombolitic deposits (Andres & Pamela Reid, 2006; Riding, 2011; Suarez-Gonzalez, Benito, Quijada, Mas, & Campos-Soto 2019). Since Archean time, microbial mats and microbialites are thought to have flourished in a wide variety of environments, ranging from marine to continental, and including hypersaline and volcanic alkaline lakes.

In the modern setting, great environmental diversification has enabled our understanding of the relationships existing between depositional setting, microbial remains, and extant communities as analogues of fossilized microbialites (Eymar et al, 2020). Present-day examples of alkaline lake microbialites include Shark Bay and Lee Stocking Island microbialites (Chagas, Webb, Burne, & Southam 2016; Kaźmierczak et al., 2011; Kremer, Kaźmierczak, & Kempe 2019). Our understanding of these modern and active microbial structures, together with their characteristic large carbonate and siliciclastic edifices have been used extensively in reconstructing the temporal and spatial distribution of early microbial communities.

Extreme physical and chemical conditions defined by the presence of  $\text{Na}^+$  as major cations, elevated  $\text{HCO}_3^-$  and  $\text{CO}_3^{2-}$ , and pH up to 9-12, promote the growth of microbial communities known as alkaliphiles in modern volcanic habitats and alkaline hot springs, where additional alkalinity is produced by the decomposition of silicate rocks (Hensel et al., 1997). These alkaline lake ecosystems are one of Earth's most productive and naturally occurring aquatic microbial mat habitats (Pecoraino & Alessandro, 2015), where alkaliphilic extremophiles survive by adapting to multiple environmental stressors, including permanently elevated alkalinity and temperatures (Schagerl & Burian, 2016). Biogeochemical co-evolution of water chemistry and microbial metabolic activities result in the abiotic and biotic precipitation of authigenic minerals as a solubility buffering mechanism, resulting in reprecipitated carbonate minerals, being the least soluble and first to precipitate (Sanz-Montero et al., 2019).



Here we present an example of an Ediacaran volcanic alkaline lake ecosystem characterized by a variety of well-preserved microbialite morphologies representing a unique and diverse community of alkaliphilic extremophiles that thrived in a caldera setting 571 Myr ago. We explore this unique late Neoproterozoic ecosystem and examine the associated biodiversity and biogeochemical developments that may have contributed to the dramatic Ediacaran biodiversification of life into complex oxygen-respiring ecosystems.

## **Geological setting**

The distinct Moroccan Anti-atlas sedimentary succession trending ENE–WSW, stretches from the shores of the Atlantic Ocean in West Africa, to the Tafilalt plain in southern Morocco (Figure 1a). The Eburnean Paleoproterozoic and Pan-African Neoproterozoic basement is unconformably overlain by an Upper Ediacaran and Paleozoic succession consisting of the thick volcanic and volcanoclastic Ouarzazate Supergroup (Thomas et al., 2002). The entire package is complicated by post-orogenic volcanic/volcaniclastic successions composed of subordinate clastic/epiclastic lithologies that unconformably overlie the Bleida and Sarhro Groups and post-structural granitoid sequences (Thomas et al., 2002). Most rocks in the Saghro inlier and the northernmost reaches of the Bou Azzer inlier, are comprised of Ediacaran volcanic rocks and clasts belonging to the Ouarzazate Supergroup associated with sub-volcanic plutons and dikes (Walsh et al., 2012). The Ouarzazate Supergroup was previously subdivided into lower volcanoclastic, volcanic and granitic lithologies labeled "XIII<sub>m</sub>", and an upper "XIII<sub>s</sub>" unit dominated by volcanoclastic and volcanic rocks isolated by an unconformity (Thomas, Fekkak, Ennih, Errami, & Loughlin 2004; Tuduri et al., 2018; Walsh et al., 2012). Most of the volcanic rocks are peraluminous to metaluminous, and range from andesitic basalts to rhyolitic lithologies with high-K calc-alkaline to shoshonitic affinities (Walsh et al., 2012). The structural, sedimentological, and volcanic features indicate subaerial effusive volcanic activity from several active centers containing calderas, and subaerial sedimentary sequences of

alluvial, fluvial and colluvial origin. The main known Caldera complexes in the central and eastern Anti-atlas are Achkoukchi in Sirwa, Oued Dar'a and Qal'at Mgouna in Jbel Saghro (Thomas et al., 2002; Tuduri et al., 2018; Walsh et al., 2012).

To the southeast of the Saghro massif (Figure 1a, b), the Ediacaran Oued Dar'a caldera in the lower Ouarzazate Supergroup consists of an enormous rectangular-shaped volcanic structure, 11 km wide and 18 km long. The caldera, situated along a northeast corridor, is composed of an incredibly well preserved infill made up of trachytic, trachydacitic and rhyolitic ash-flow tuffs ponded within a large volcano (Walsh et al., 2012). The northeast margin is intruded by pink granite interpreted as parent magma of the volcanic rocks (Figure 1b). The southwestern margin (Choubert and Faure-Muret, 1970) is marked by a 200 m coarse-grained, quartz-rich, and granulated volcanoclastic deposit resting on the caldera's infill ash-flow tuff that is intercalated with lacustrine beds containing purplish-green microbialites (Álvaro et al., 2010; Walsh et al., 2012; Álvaro & González-Acebrón, 2019). The age of the caldera infill has been estimated to the last major volcanic eruption from the caldera  $\sim 571 \pm 5$  Ma according to Walsh et al., 2012 (Figure 1b).

This study is focused on the Amane Tazgart carbonates located on the western edge of the Saghro inlier (Figure 1b, c), located  $\sim 25$  km southeast of the Ouarzazate classical geological fieldtrip stop along the Ouarzazate–Zagora Agdz road (*e.g.*, Choubert & Faure-Muret, 1970). Choubert and Faure-Muret (1970) were the first to propose a lacustrine depositional setting for these meter-thick, carbonate-bearing volcano-sedimentary units, in view of their restricted geographic expansion and the obvious nearness of domal and conical stromatolites. The development of the Amane Tazgart microbialites was controlled primarily by the caldera's volcanic and geothermal activity, combined with silicate hydrolysis under subtropical conditions (Álvaro et al., 2010; Álvaro & González-Acebrón, 2019).

## **Materials and Methods**

Field mapping, logging, sampling and facies analysis were conducted during two field trips involving two sections and 49 samples. Thin sections were produced for detailed petrographic observations with a ZEISS Discovery V8 microscope equipped with an AxioCam ERc 5s camera at the University of Poitiers. Mineralogical composition was investigated by X-ray diffraction (XRD) on a subset of 25 representative agate mortar powdered samples. The samples were analyzed with an Xpert Pro Bragg/Bentano diffractometer at the University of Poitiers using CuK $\alpha$  radiation operating conditions of 40 kV and 40 mA. Powdered samples were analyzed at the 2 to 65° 2 $\theta$  angular range, using 0,017° 2 $\theta$  step sizes per 0,7 s. After air drying, ethylene glycol solvation, and heating at 350°C and 550°C, the clay fraction was analyzed over an angular range of 2–35° 2 $\theta$  at 0,017° 2 $\theta$  using 0,7 s step sizes. Mineralogical identification was performed using the Xpert High-score pro software by comparing the data to the International Centre for Diffraction Data (ICDD) database (*e.g.*, Moore & Reynolds, 1997).

A sample from each facies type was hand-crushed to 1-5 particle cm size and dissolved in 10% diluted acetic acid for 8 to 24 hours, for microfossil analysis. Suspected microfossil remains were picked out from the acid residues using a stereoscopic microscope and then imaged at high resolution with scanning electron microscope EDAX-AMETEK SPEC\_007 at Cadi Ayyad University, Morocco and with JEOL JSM IT 500 at Poitiers University, France.

### **The Ediacaran Amane Tazgart microbialites**

#### ***General description***

The Amane Tazgart succession forms a lens-shaped unit, is less than 1 km wide and up to ~15 m thick in the central part (Figure 1c). The succession is less folded, slightly dipping WNW and divided by a NNE-SSW fault into two compartments (Figure 1d). It is underlain by grey aphanitic andesitic magmas and overlain by a volcano-sedimentary succession including

andesitic lava flows, peperites and epiclastic micro-conglomerates and sandstones rich in volcanic clasts. The surrounding depositional setting dominated by subaerial volcanic and sedimentary setting of the Oued Dar'a Caldera, as well as the overall facies features of the Amane Tazgart, suggest short periods of attenuated volcanic activity that are accompanied by lacustrine sediment deposition in ephemeral ponds (*e.g.*, Álvaro et al., 2010; Álvaro & González-Acebrón, 2019)

The lower boundary of this succession is erosional and locally preserves lens-shaped conglomerates and narrow trough fillings (Figure. 1c). The investigated clastic and carbonate layers overlying the conglomerates along the whole area of Amane Tazgart show lower and upper packages preserving diverse varieties of microbialites and associated non-microbialitic deposits (Figure 2). The lower part consists of four sequences, decimeter to meter thick, each ending with beds of microbialites numbered in the measured section as H1 to H4. In general, the first sequence starts with irregular patchy clotted thrombolites and stromatolites (Figure 2), overlain by thick pale cream bioherm layers that coalesce to form the wide H1 domes. The H2-H4 microbialitic layers in the overlying sequences are preceded by clastic carbonates containing rippled sandy calcarenites, cross-bedded, and graded calcirudites dominated by clast-derived microbialites, and cm-thick interbeds of fine-grained laminated sandstones and siltstones. Within the microbialitic and non-microbialitic deposits, carbonate spherulitic grains occur in both the clastic and carbonate lithologies. The Upper section forms a widespread meter-thick layer along the Amane trough and consist of planar laminated and rippled medium to fine-grained epiclastic sandstones and siltstones dominated layer. These are overlain by the last microbialitic horizon H5 that preserve vertically trending stromatolites and laminations buried by peperites and the overlying volcano-sedimentary rocks.

#### **Amane Tazgart microbialites: morphotypes and fabrics**



### ***Patchy thrombolites and microstructures***

The lithological features of the Amane Tazgart microbialites, distinguish thrombolitic, stromatolitic, and composite microbialites made largely of domal carbonaceous and clastic stromatolites (Figure 2).

The thrombolitic microbialites are built on a framework characterized predominantly by mesoclots, matrix cement, and voids. One type of mesoclots appears frequently in the sampled sections, being commonly irregular to patchy in shape (Figure 3a, b). A matrix composed of fine-grained epiclastic sediments filled the spaces between the mesoclots, and appears reddish to purplish on fresh and polished surfaces (Figures 3a, b). The thrombolitic voids are usually filled with light sparitic cement that is locally replaced by late diagenetic microcrystalline quartz.

Microscopically, the mesoclots are characterized by clotted to peloidal micrite, with some scattered sand- to silt-sized clastic grains of quartz, feldspar and iron-impregnated volcanic composition. The mesoclots are surrounded by fan-shaped to botryoidal calcite cement (Figure 3c). Occasionally, mesoclots preserve faint relatively thin laminations, which consist of alternating sparitic and clotted micritic laminae (Figure 3d). The matrix is mainly epiclastic, and partially silicified. In some cases, sediments between the mesoclots contain distinctive wavy and wrinkly laminations expressed as wrinkly-crinkly dark clastic grain-trapping laminae (Figure 3e).

### ***Composite domal microbialites***

Composite microbial structures between the thrombolites and stromatolites are common (Figure 3f), making up the principal structure of horizons H1 and H3. The composite framework within each dome can be observed at distinct scales, with the stromatolitic fabric dominating in many domes whereas the thrombolitic forms are isolated in small domes at the base and/or in

the patchy and irregular layers that are draped and encrusted by stromatolites (Figure 3f, g, h). Centimetric non-branched columns were identified intermingling with the patchy clots, while the microstructural fabric holding the thrombotic mesoclots together, preserve typical clotted to peloidal micrite. Thin laminated stromatolites and occasional peloids fill the inter-mesoclots spaces (Figure. 3h). The dominating laminated fabrics in these domes display grain-sized, micritic fine-grained, and sparitic laminae. The grain-sized laminae preserve wrinkled features and form lens-shaped layers with quartz, feldspar and volcanic clasts embedded in a partly silicified amorphous matrix (Figure 3i). The micritic finer and dark laminae, may contain sparse and fewer finer clastic grains, are continuous, sometimes lenticular, and characterized by a dense fabric. The sparitic laminae are the lightest in color and constituted of well-crystalized abiogenic sparry layers (Figure 3f).

#### ***Flat large domal stromatolites***

This morphotype occurs along two beds and are up to 30 cm thick, within the microbialitic H2 and H4 horizons (Figure 2). At the field scale, they correspond to flat and large laterally linked stromatolitic domes of up to 1 m in diameter (Figure 3j). Internal laminations are very fine, showing regular and typical wavy and crinkly features (Figure 3k), consisting of alternating dark micritic to microsparitic light laminae, grainy calcitic laminae and iron crusts enhanced by tufted microbial mats. Tufts form vertically oriented cone shaped laminae induced by the growth of the filamentous microbial communities (Gerdes, 2010; Gerdes, Klenke, & Noffke 2000). They are typically 0.02 cm in height but can grow to 0.1 cm (Figure 3l), and are internally filled with fine to medium-grained sediment and macro-sparitic calcite.

#### ***Clastic dominated stromatolites: morphotypes and microstructures***

The clastic dominated stromatolites appear in microbialitic horizon H5. They form a single bed up to 2 m in thickness, and preserve a succession of four morphotypes ranging from flats to crinkly laminated domes, cones, and laterally linked hemispheroidal columns. The flat to

crinkly laminated framework consisting of sub-millimeter lamination appears in the lower parts of the stromatolitic bed (Figure 2). In the upper section, the planar laminated stromatolites occupy the interdome troughs, forming layers of up to 10 cm thick which grade vertically into small domes of up to 5 cm in diameter (Figure 4a). Domes up to 0.5 m high (Figure 4b) and 30 cm wide, together with conical morphotypes reaching heights of 0.1 m and varying widths of 0.1-0.2 m (Figure 4c), occupy the upper thick portions of horizon H5. The last morphotype consists of laterally linked hemispheroidal structures, which overlay the flat laminated stromatolites. The hemispheroidal features appear spaced on bedding surfaces and preserve subcircular to elliptical sections with diameters ranging from 5 to 8 cm (Figure 4d, e). The vertical section shows inclined to elongated hemispheroids with a NW-SE general trend similar to that of the wave ripples in the underlying clastic rocks. The propagation and scattering of big composite domes composed of laminations with circular axial column patterns that transition to a wavy architecture at the margins, suggest strong competition for space and growth (Figure 4f). The various stromatolitic structures grew inside large metric domes or biostromes, of a thickness varying between 1-1.2 m, while the flat-laminated to pseudo-columnar stromatolites that developed in the interdome spaces, tend to alternate with red epiclastic sands that filled the interdome spaces.

In thin section, the biolaminations in the clastic stromatolites consist of alternating medium sand-sized to silt-sized clastic, micritic, iron-stained and sparitic laminae. The grainy laminae forming the main component of these stromatolites (Figure 4g) preserve a wavy and wrinkled-crinkled fabric, formed by medium to coarse-grained epiclastic grains and tuffs with lots of feldspar derived from the surrounding volcanic rocks, including iron, rock fragments, and clay minerals. The micritic laminae are represented by a dense fabric composed of scarce oxides, feldspar and peloidal laminae (Figure 4h, i). The color of micrite varies from brown to brownish red depending on the proportion of iron and clay minerals, where increasing iron enrichment

and clay content are associated with a darker coloration (Figure 4h, i), with the iron-rich layers being the darkest (Figure 4g). These iron-rich layers consist of thin laminae that are less than 1 mm thick, composed of iron and volcanic grains and sometimes represent the main crusts between the clastic rich laminae. The sparitic laminae correspond to well crystalized, essentially, abiogenic sparry layers (Figure 4h).

Noticeable, are almost perfectly rounded features encased by contorted dark laminae, identified in the flat domal and conical stromatolites. Most of these features ranging in size from 3-100  $\mu\text{m}$  are partially filled by diagenetic microcrystalline quartz (Figure 4j). Other features supporting gas production beneath the mats are vertically oriented ptymatic veins cutting the biolaminations, interpreted as gas-escape structures. These laminations are arranged into layers corresponding to those defined by Monty (1976) as repetitive and alternating, with most belonging to the composite alternate type (Figure 4k). The grain-sized sparitic or micritic and sparitic laminae form the frequently observed alternating laminations (Figure 4h, k). On the other hand, the light sparitic layers containing thin peloidal micritic laminations and sparite are associated with composite-style laminations, while micritic/organic crusts separate repetitive laminations in the grain-sized beds (Figure 4l).

## **Non microbialitic deposits**

### ***Calcirudites with microbialite-derived clasts***

Several lens-shaped coarse-grained layers of poorly sorted microbialitic clasts are interbedded with the microbialitic deposits, and contain clasts ranging in size from 0.3-2 cm. The shapes of the clasts distinguish subrounded and flat-pebble dominated calcirudites clasts (Figure 5a-b). The flat-pebble rich calcirudites suggest on-site deposition and weak reworking of lithified microbialites, while the subrounded microbial clasts indicate strong reworking by wave induced currents. These sediments are interrupted and intermingled with centimeter-thick stromatolitic



laminations interpreted as representing conditions suitable for microbialite development being frequently interrupted by energetic currents.

Polished slabs show that most of the microbialitic clasts still preserve their primary features with clotted or laminated fabrics, some of them being partially or fully replaced by white diagenetic calcite (Figure 5a, b). The matrix consists of sand to silt-sized epiclastic sediments embedded in a microsparitic cement, and mostly derived from the reworking of the surrounding andesitic rocks (Figure 5a, b). Microscopically, the stromatoclasts alternate in composition from dark peloidal and clotted micritic to light microsparitic laminae. Medium coarse-grained epiclastic sediments cemented with microcrystalline quartz, occupy the spaces between the stromatoclasts, while sparitic calcite fills the remaining voids.

#### ***Spherulites and spherulitic fabric.***

Red facies composed of fine to coarse-grained sandstones, full of spherulites, and poorly sorted microbialitic clasts (Figure 5c), occur in the basal part of the thrombolitic and composite microbialitic layers. Being spherical to oval, and ranging from 1 to 5 mm in diameter, the spherulites commonly develop into masses of deviated structures (Figure 5c). In thin section, the spherulite grains comprise fibro-radial and fan-shaped calcite crystals coating the nuclei that are generally darker than the cortex. These nuclei are composed mainly of micrite-microsparite cement and sometimes mixed with clastic elements similar to those of the surrounding matrix (Figure 5d).

#### ***Rippled and parallel laminated sandy calcarenites***

These deposits occur within the microbialitic carbonates, with beds attaining heights of 30 cm. Internal structures consist of superposed sets of current and climbing ripple laminations. Occasionally, centimeter-thick stromatolitic laminations occur on top of the beddings planes, indicating limited microbial mat growth during low energy conditions (Figure 5e). The

stromatolitic layer preserves sub-millimetric wrinkly and crinkly laminations that alternate with coarse/fine-grained micritic laminae occasionally stained with iron (Figure 5f).

### ***Clastic sediments***

A sedimentary package of alternating rippled and parallel laminated epiclastic sands and shales, separates the carbonate and clastic units. These deposits display sedimentary features including ripple marks, crescent and mat-related structures (Banerjee et al., 2010). The ripple marks (Figure 6a) tend to change direction from layer to layer, suggestive of persistent turbulence. The MRS exhibits a wide range of surface morphologies related to mat-growth, mat-induced, and mat-protected structures (e.g., Riding, 2011). The Amane Tazgart MRS features exhibit domal sand buildups or stromatolitic sandy bedding surfaces on the sandstones (Figure 6b) with varying sizes. Grouped and ungrouped structures, which may occur on the same sandstone bedding surfaces, are protected in curved hyporelief on the soles of the overlying sandstone beds (Bottjer & Hagadorn, 2007). The crescent-shaped morphologies identified on the bedding surface of one sandstone bed (Figure 6c), show vertically oriented fluid escape structures filled with gas bubbles that impart a domal to conical shape to the superposed laminae (Figure 6d).

### ***Peperites***

The clastic stromatolitic domes are covered by peperites intermixed and intermingled with unconsolidated sediment and magma, considered as good evidence for unconsolidated and poorly consolidated wet sediments (e.g., Skilling, White, & McPhie 2002). These peperites are further linked to epiclastic sediments that are displaced by and trapped in lava flow (Figure 6e, f), including decimeter-thick globular andesitic lavas that are characterized by the upwards formation of elongated centimeter to decimeter sized clasts with increasing lava compositions (Figure 6e).

### **Mineralogy**

The bulk mineralogy of the studied sections is predominated by calcite, quartz, plagioclase, and occasional illite and hematite (Figure 7). Detrital particles are present in all the microbialites and detrital facies, including K-feldspar, plagioclase, and hematite. We observe that the mineralogical composition of both the Amane Tazgart sections has changed since deposition first took place. In the lower sections (Figure 7a, b), calcite is predominant over quartz, in both the microbialitic (Figure 7a) and the non-microbialitic facies (Figure 7b), while the opposite occurs in the upper sections (Figure 7c, d). Clay mineralogy shows that illite and/or mica and chlorite are predominant (Figure 7). However, the mineralogical evolution through these two phases is unclear as indicated by the weak 001 reflection intensities. The <2  $\mu\text{m}$  clay size fractions show a predominance of chlorite, mica/illite, and chlorite/smectite (C/S) mixed-layer minerals (MLM) (Figure 8). This is dominated by chlorite and a fairly low degree of bulk organization at the base of the section in both, the microbialitic and the non-microbialitic layers, as indicated by a 15 Å peak in the ethylene-glycol treatments and a superlattice reflection of 25-30 Å (Figure 8a, b). Upward, the MLM is increasingly enriched in smectite, with bulk organization of the C/S ratios shown by superlattice reflections of 29-30Å (Figure 8c- d).

### **Biogeochemical reconstruction**

Following acetic acid dissolution of carbonates, several aggregates picked out and thoroughly examined by SEM-EDS, resulted in the identification of spherical, globular and irregular morphologies (Figure 9) similar to those described in modern microbial aggregates (Xiao, Li, & Reynolds 2018). Although only minor in occurrence, the elongated shapes are prevalent while the aggregates are mainly found associated with the spherulitic samples and occasionally within the thrombolites. Several aggregations are joined together by smooth mucus-like structures that sometimes drape the aggregates (Figure 10a-c). EDS analysis of the non-coated aggregates, reveal silica and a significant proportion of carbon (Figure 10d Spot 1), while the smooth mucus-like structures are composed mainly of carbon and sulfur, with a proportion of

silica, magnesium, arsenic and chlorine (Figure 10d-Spot 2). High-resolution SEM observations show the presence of globule-like and coccobacilli-like crystals, which resemble the remains of coccoidal and coccobacilli-like cyanobacteria. They occur within EPS-like material, display a size range of 1-2  $\mu\text{m}$ , and have affinities similar to those described by Chafetz, Barth, Cook, Guo, & Zhou (2018). These crystal structures preserved in silica contain a significant proportion of carbon and sulfur (Figures. 11a, Spot 1, Spot 2).

A representative sample from each facies, studied for ultrastructural characterization of the microbialites, and SEM examination of the thrombolitic samples, revealed numerous micropores mainly embedded in the calcitic crystals, indicative of potential bacterial molds (Figure 11b) and consistent with a microbial size range of 0.5-2  $\mu\text{m}$  (Tang, Shi, & Jiang, 2013). Although not unique to any known microbial morphotype, our observations are coherent with Proterozoic micritic and peloidal limestone facies, and when compared to modern analogues, their deposition has been strongly linked to the activity of cyanobacteria, with coccoidal forms represented by cell casts (Dongjie et al., 2013, Tang, Shi, & Jiang, 2013).

EDS analysis of the dark stromatolitic laminae, revealed clay minerals superimposed on each other, with no significant differences observed between the stromatolitic and thrombolitic facies (Figure 11c). The calcitic zones are always composed of micropores, and dark clayey laminations. Three-dimensional analyses of the spherulitic samples show calcitic wedges with rounded micritic nuclei representing chemical compositions different from the cortices. The cortices are composed of pure calcite ( $\text{CaCO}_3$ ), while the nuclei are composed of calcite associated with clays represented by Si, Al, K and iron, which explain the darker light attenuated composition of the nuclei in thin section (Figure 11).

## Discussion



*Environmental controls on the genesis of the microbialites*

The harsh living conditions of alkaline volcanic lakes push organisms towards extreme physiological adaptations that enable and enhance the survival of specialized alkaliphilic populations. These microorganisms innovate resilient intra-cellular metabolic processes to overcome external physico-chemical stressors like high turbidity, dramatic increases in pH, elevated concentrations of toxic trace elements and metals, and the dramatic effects of extremely high temperatures on cell homeostasis, physiology and function (Schagerl & Burian, 2016). Studies on modern alkaline lake ecosystems, demonstrate that microbes handle these persistent extreme environmental conditions through regulatory, conformity and avoidance processes (Willmer et al., 2004). The Amane Tazgart microbialites give new insights to the existence of successful and high productive terrestrial volcanic ecosystems during the Late Neoproterozoic that would have actively contributed towards the transformation of the Ediacaran biosphere, by for example, through oxygen and organic matter production.

The facies described in the Amane Tazgart succession, as well as the overall geodynamic setting, point to a terrestrial lacustrine setting with active microbial communities that played a crucial role in local biogeochemical cycles and redox. The microbialitic successions are encased in a volcanic complex exhibiting evidence of subaqueous explosive and effusive volcanic activities. Additionally, the sedimentary and volcano-sedimentary features indicate deposition in an alluvial and colluvial environment (Álvaro et al., 2010; Tuduri et al., 2018; Walsh et al., 2012). The microbialitic and non-microbialitic features, together with the vertical arrangement of the facies, indicate low-energy lacustrine conditions punctuated by high-energy events. The high-energy stages are associated with erosive currents producing mainly coarse-grained clastic carbonates dominated by ripped-up microbialitic clasts and wave-generated currents associated with cross-bedded calcarenites, planar laminated and wave-rippled sandstones. The low-energy conditions favored lake floor colonization by microbial mats, to produce at the incipient stages

patchy and irregular thrombolites and stromatolites overlain by large and coalescent dome-forming bioherms. The microfabric in the microbialitic carbonates and clastic stromatolites indicate the trapping and binding of sediments during critical intervals of low clastic input into the lake, suggesting that microbial oases flourished in the lake during short periods coincident with attenuated volcanic activity. The demise of this lake system and its microbial community occurred during an andesitic lava flow event, indicated by the peperitic facies blanket associated with horizon H5. These andesitic lavas provide a maximum age of  $571 \pm 5$  Ma, which is the age of the last major volcanic eruption from the caldera (Walsh et al., 2012).

#### ***Microbialite growth morphologies and environmental implication***

The subdivision of the Amane Tazgart section into a lower microbialitic and clastic carbonates, and an upper of clastic stromatolites and sandstone sections, separated by a meter-thick clastic layer composed of sandstones, and overlain by clastic stromatolites, is interpreted to imply significant chemical change and clastic sediment supply to the lake. This transition may be related to water depth fluctuations and calcium carbonate saturation. The vertical facies trends along the succession show sequences starting with shallow high-energy littoral deposits, and grading upwards into microbialites growing in quite-energy conditions. Such sequences, as well as the caldera setting, indicate limited water supply from runoff and active streams generally lacking in caldera ecosystems. In modern calderas and crater lake locations, water level fluctuations are mainly influenced by groundwater supply, hydrothermal springs, evaporation, and water supply to evaporation rate ratios (*e.g.* Pecoraino & Alessandro, 2015). Calcium carbonate saturation decreases from bottom to the top of the succession as indicated by the transition from calcite-dominated to quartz-dominated deposits (Figure 2). The shift in facies composition from carbonate-dominated to clastic-dominated fabrics, appears to be related to hydrological regime changes influenced by surficial water supply. It is also possible, and as demonstrated in modern situations, that some parameters like alkalinity, water temperature and

438 biological processes may have controlled carbonate saturation and precipitation (*e.g.*, Kremer,  
439 Kaźmierczak, & Kempe 2019) .

440 The association of clotted and laminated textures in the composite microbialites, imply  
441 variation of growth styles in the same environment, and suggests a complex transaction between  
442 processes favoring thrombolitic and stromatolitic textures that cannot be explained by simple  
443 changes in environmental conditions (Harwood & Sumner, 2011). On the other hand, the  
444 relative proportion, distribution and upward increase of stromatolitic fabrics at the expense of  
445 the thrombolitic communities, can be attributed to local environmental variations within the  
446 same broad environment. Thus, this co-occurrence of clotted and laminated fabric may suggest  
447 that the different textures are the result of simultaneous growth of morphologically distinct  
448 microbial communities (Harwood & Sumner, 2011), and that stromatolitic communities  
449 became more dominant with the age and the chemical evolution of the lake, and became the  
450 last community to finalize the construction of the epiclastic stromatolitic horizon.

451 Upon appearance, the stromatolitic features in the clastic horizon produce flat shallow water  
452 morphologies, which we link to frequent sediment supply, sediment composition, and grain size  
453 distribution (Andres & Reid, 2006). The change from flat to columnar stromatolitic  
454 morphotypes has previously been considered to indicate an upward deepening sequence  
455 associated with occasional sand burial which leads to the development of columns (Andres &  
456 Reid, 2006). However, the change from columnar to domal stromatolitic forms has also been  
457 related to a deepening event (Adachi et al., 2019), while progression from columnar to dome-  
458 shaped stromatolitic environments was further interpreted as a feature of sediment flux rates  
459 (*e.g.*, Planavsky & Grey, 2008). Consequently, the enrichment of detrital materials in the  
460 columnar and dome-shaped morphotypes, implicate the influence of sediment flux rates on the  
461 development of the stromatolitic morphologies. Vertical column diameter changes, reflect  
462 microbial activity, following small-scale environmental fluctuations. When microbial activity

weakens, the upward growth of stromatolites is compensated by a decrease in diameter (Adachi et al., 2019). Furthermore, bridges develop between cyanobacterial columns and domes when microbial activity intensifies in abundant sunlight to generate sufficient photosynthetic energy to enable the extension of mats across the individual columns and the sediment-filled cavities between them (Adachi et al., 2019).

The presence of C/S and MLM clays minerals in the microbialitic and non-microbialitic facies, is a feature of hypersaline environments, hydrothermally altered basalts and ultrabasic rocks, burial diagenesis of volcanoclastics, graywackes, and contact metamorphism (Środoń, 1999 and references therein). In our case, there was no petrographic evidence for metamorphic alteration. Therefore, the presence of C/S MLM in all the facies is most parsimoniously interpreted as related to the hyper salinity of the lake, and/ or to burial diagenesis.

The revelation of smooth mucus like structures, their shape and composition, point to a likely EPS provenance, similar to those reported in Mesoproterozoic thrombolites from China (Dongjie et al., 2013). They share many similarities in terms of size and morphology, with mineralizing EPS reported in hypersaline microbial mats from Qatar (Perri et al., 2018). The Ca, Si, Al, S and Mg concentrated in the EPS-like remains, typically contribute to EPS mineralization and preservation in sediments (Perri et al., 2018). Similarly, potential As enrichment by EPS has been associated with Archean and Proterozoic microbialites (Sforna et al., 2017; Aubineau et al., 2019), as in our samples and EPS from modern microbial communities living in hypersaline lakes associated with photosynthesis and volcanic activity (Sforna et al., 2017; Sancho-Tomás et al., 2018).

Spherulites are composed mainly of calcite crystals and are associated with thrombolitic and composite microbialites, where the main mineralogical phase is carbonate, which is necessary

for the development of spherulites. In epiclastic stromatolites, the main mineralogical phase is quartz, with only traces of carbonate minerals, which may explain their lack of spherulites. Spherulites formation was previously related to microbial activity, through association with the presence of EPS which generated favorable microenvironments for calcium carbonate precipitation at the sediment–water interface, or just beneath the sediment-water interface (e.g., Kirkham & Tucker, 2018; Mercedes-Martín et al., 2016). Further, Mercedes-Martín et al. (2016) revealed typical spherulitic-radial calcite developing in saline alkaline water and in the presence of specific dissolved organic acids, which are strong constituents of EPS. Nevertheless, an abiotic origin for spherulites has been related to changes in lake chemistry, including temperature, pH, and Si, Mg and Ca fluxes (Wright & Barnett, 2015). Abiotic formation of spherulites inside a suspension of poorly crystalline Mg-Si gels has been reported in soda lakes when long-term evaporative water loss builds sufficient dissolved Si and Mg to elevate Mg-Si gel precipitation (Wright & Barnett, 2015). However, our case lacks evidence in support of the predominance of Mg-Si mineral phases. Instead, extracellular polymeric substances are associated with the spherulitic, as well as the thrombolitic and composite microbialitic assemblages. Taken together, the highlighted necessity of EPS in the precipitation of spherulites, EPS elemental properties, and occurrence in analogue modern environments similar to our Ediacaran setting, strongly support the biogenic origin of the mats. Importantly, EPS is a major factor in the formation of microbial aggregates and crucial for maintaining the three-dimensional structure of microbial biofilms (Sheng, Yu, & Li 2010).

The gas-bubble sizes in the Amane Tazgart microbialites, and their near-perfectly round shape, is consistent with those depicted in modern and ancient mat-related structures and stromatolites (Aubineau et al., 2019; Bosak et al., 2009; Sallstedt, Bengtson, Broman, Crill, & Canfield 2018). Tufted structures and gas-bubbles are commonly tied to high oxygenic photosynthetic activity, generated by cyanobacteria, interpreted to indicate sufficient gas accumulation to

overcome considerable hydrostatic pressure at depth (Bosak, Liang, Min, & Petroff 2009, Bosak et al., 2010). Furthermore, experiments with laboratory-grown cyanobacterial mats suggest that both mat-trapped and mat-attached bubbles are saturated with O<sub>2</sub> compared to the overlaying atmosphere. Hence gas bubbles in sedimentary rocks are primarily interpreted as remnants of oxygenic photosynthetic activity against non-photosynthetic gases (Bosak et al., 2010). A study of Antarctic microbial mats from Lake Fryxell, report cyanobacteria developing O<sub>2</sub> oases in benthic microbial mats, even at very low net photosynthetic rates of 0.05 μmol O<sub>2</sub> m<sup>-2</sup>s<sup>-1</sup> at 9.8 m (Sumner, Hawes, Mackey, Jungblut, & Doran 2015). By implication, the abundant bubbles in our mats suggest high oxygenic photosynthetic rates likely dominated by alkaliphilic cyanobacteria, pointing to environmental radiation and habit specialization in the cyanobacteria by the Ediacaran time.

Further, the data hint that extreme alkaline lake environments like those of the photosynthetic mono lakes of California where volcanic arsenic fuels anoxygenic photosynthesis (Kulp et al., 2008; McCann et al., 2016), may have been a common feature of the Ediacaran biosphere. Intriguingly, As is associated with our EPS material, with elevated levels proposed for the Ediacaran biosphere (Chi Fru et al., 2015), where strong resilience to As detoxification would have been a key requirement for survival (Chi Fru et al., 2018).

#### ***Microbialites and diagenesis***

Álvaro & González-Acebrón (2019) have characterized a number of diagenetic aspects in the Amane Tazgart microbialites similar to other sections of the Anti-atlas. They described several early-diagenetic processes, punctuated by polyphasic fissuring related to hydrothermal activity, with the generation of fibrous, botryoidal and blocky/drusy mosaic calcites, idiotopic mosaics of dolomite, and euhedral to drusy calcite produced by dedolomitization. They recognized silicification as early diagenetic occlusion of sediment/water interface interparticle porewater spaces within a pyroclastic rock setting, and hydrothermal silica precipitation in secondary

pores (Álvaro & González-Acebrón, 2019), consistent with our observations. We note that intraparticle pores in the carbonate units were filled mainly by sparite, unlike those in the clastic stromatolites that are filled by early diagenetic microcrystalline quartz. This observation provides support for an initial carbonate-rich water column that subsequently developed to enrich silica at the expense of calcite. The carbonate armor of the first microbialitic unit makes them unstable and strongly vulnerable to diagenetic processes and hydrothermal activity. On the other hand, the clastic stromatolites confer more resistance, indicated by their restriction to early diagenetic silicification and hydrothermal silicification.

## Conclusions

The Amane Tazgart succession provides an example of early cyanobacteria radiation and habitat specialization. Several modern examples in similar “volcanic lake” settings are well studied and host mainly extremophilic microbial communities specialized to extreme environmental conditions, which include among others, elevated alkalinity, salinity and temperatures (Merino et al., 2019; Pecoraino & Alessandro, 2015). It was not until towards the end of the Ediacaran that some of the most rudimentary forms of complex animals first appeared, implying a bulk of Earth’s history has been dominated by microbial life, stretching back to the Archean (*e.g.*, Knoll, Bergmann, & Strauss 2016; Van Kranendonk et al., 2019). Remnants of Archean life have been described from volcanic settings as microbially related deposits and structures preserving evidence for their biogenicity (Hickman, Cavalazzi, Foucher, & Westall 2018; Stüeken & Buick, 2018; Van Kranendonk et al., 2019). The Amane Tazgart succession highlights an exceptional Ediacaran case predating the Cambrian explosion, providing a snapshot of a functioning microbial ecosystem in a terrestrial volcanic habitat. The sedimentary features indicate a shallow lacustrine setting and deposition in a narrow-closed system with negligible stream and riverine input, recharged being most likely by hydrothermal

inflows and seasonal runoff. The development and preservation of putative microbial structures that flourished during short intervals of non-volcanic activity and suitable taphonomic conditions, including early lithification, provide strong support for the volcanic environment in which the mats grew, while at the same time constraining the taphonomic conditions that enabled the remarkable preservation of these alkaline lake biota, including features pointing to oxygenic photosynthesis.

The fossilized aggregates, the biogenic origin of the associated facies, silicification, the presence of EPS, and their Ediacaran age, lead us to propose the aggregates as either bacterial microcolonies or silica mineralized cell aggregates. See for example Xiao, Li, & Reynolds (2018) for a comparison. The data further demonstrate that the 571 Myr old Ediacaran Amane Tazgart alkaline lake supported a unique and diverse community of extremophiles specialized to thrive in equally unique high alkalinity terrestrial aquatic ecosystems. Particularly, the combined observation of geological indicators for oxygen production, with sedimentary abundance of stromatolites and their remarkably well-preserved gas escape structures and bubbles, highlight the radiation and spread of alkaliphilic oxygenic photosynthesizers to extreme alkaline environments since Ediacaran time. These organisms certainly contributed towards the oxygenation of their terrestrial lake ecosystem habitats, raising fundamental questions about the contribution of the terrestrial biosphere to Precambrian atmospheric oxygenation and to early nutrient biogeochemical cycles.



## Figure captions

**Figure 1** (a) Geological map of the Anti-atlas of Morocco. (b) Structural Map of Oued Dar'a caldera. (c) Geological Map of Amane Tazgart's microbialites. (d) Geological cross-section of Amane Tazgart site.

**Figure 2** Detailed lithostratigraphic column of the Amane Tazgart biofacies. Chlorite (Chl), Illite (Il), mixed-layer minerals (MLM) and chlorite/smectite (C/S), represent the Clay mineralogical assemblages of the various microbialitic facies.

**Figure 3** (a) Thrombolitic facies with irregular to patchy shaped mesoclots. (b) Polished slab of (a). Mesoclots (Ms). Silicified matrix (Sm). (c) Thin-section photomicrograph of thrombolites (Cm= clotted micrite, Ce= botryoidal calcite cement). (d) Thin-section photomicrograph of laminated mesoclots constituted with alternate light sparitic and peloidal micritic laminae. (e) Thin-section photomicrograph of laminated matrix in thrombolites. (f) Field view of composite microbial structure between thrombolites (Cl=clotted fabric) and stromatolites (Lm=laminated fabric). (g) Polished slab from same sample as panel f. (h) Thin-section photomicrograph of a composite microbial structure showing mesoclots (Cl) draped by a laminated fabric (Lm). (i) Thin-section photomicrograph of the laminated fabrics in composites microbialites constituted of alternating grain-sized (Gs), sparitic (Sp), and micritic laminae (Mi). (j-k) Flat to large domal carbonate stromatolites. (l) Thin-section photomicrograph of flat to large domal stromatolites showing wavy-crinkly aspects between iron crusts micritic laminae (Mi) and sparites (Sp). The white arrow shows tufted microbial mats. The coin is 2.4 cm in diameter.

**Figure 4** (a) Laminated to pseudo-columnar stromatolites. (b) Stromatolitic dome, (c) cones. (d) vertical columns, (e) tilted columns. (f) composite dome with laminations first developing in circular patterns in the axial part of the column before transitioning to progressively wavier architecture towards the margins. (g) Thin-section photomicrograph of alternating grain-sized (Gl) and iron rich laminae (Ir). (h) Thin-section photomicrograph of alternating micritic (Mi) and sparitic laminae (Sp). (i) Thin-section photomicrograph of a peloidal to clotted micritic laminae. (j) Thin-section photomicrograph of fossilized gas bubble structure (yellow arrow). (k) Thin-section photomicrograph of composite alternate type laminae between light sparitic and dark wrinkled-crinkled grain-sized laminae. (l) Thin-section photomicrograph of repetitive style laminae. Pen is 15 cm long. The coin is 2.4 cm in diameter.

**Figure 5** (a) Polished slab of flat pebble calcirudite, (b) Polished slab of rounded shape microbial clasts in a calcirudite. (c) Polished slab of the spherulitic facies, showing spherulites (arrow) and microbial derived clasts=Mc. (d) Thin-section photomicrograph of spherulites embedded in an epiclastic sand-sized matrix, containing a spherical spherulite with a clastic nucleus, surrounded by coarse-grained wedge-shaped calcite crystals (1), and an oval spherulite (2) with a micrite-microspar core (dashed lines). (e) Rippled sandy calcarenites covered with stromatolitic layers. (f) Thin-section photomicrograph of the microbial lamination of (e) showing coarse-grained microbial mats, and wrinkly-crinkly iron rich laminae.

**Figure 6** (a) Ripple marks structures. (b) Domal sand buildups (arrows). (c) Crescent structures (dashed lines). (d) Thin-section photomicrograph of gas escape structure in a crescent shape structure. (e) Globular peperites superposed with fluidal elongated lava clasts (dash lines outline globular lava clasts). (f) Thin-section photomicrograph of a peperites showing the epiclastic nature of sediments=Sd, surrounding volcanic clasts=Vo. Pen is 15 cm long and coin 2.4 cm in diameter.

631  
632 **Figure 7** (a) Bulk-rock X-ray diffraction patterns of thrombolites, (b) Bulk-rock X-ray  
633 diffraction patterns of a clastic deposit associated with thrombolites. (c) Bulk-rock X-ray  
634 diffraction patterns of clastic stromatolites. (d) Bulk-rock X-ray diffraction patterns of clastic  
635 sediments within stromatolites, Chlorite=C, Calcite=Ca, K- Felds=F, hematite=He, illite=I,  
636 plagioclase=P, quartz=Q). Red areas designate the highest peak of calcite minerals, while green  
637 areas indicate the apogee of quartz minerals.

638 **Figure 8** XRD diffractogram of air dried (1) ethylene-glycol solvation, (2) thermal treatment  
639 at 350°C, (3) et 550°C, (4) of microbialitic, and detritic samples. (a) XRD diffractogram of the  
640 microbialitic horizon H1 located at the base of the section showing a C/S MLM dominated by  
641 chlorite as indicated by a peak of 15 Å in ethylene-glycol treatment (red circle). (b) XRD  
642 diffractogram of detritic facies at the base of the section similar to observations in panel (a).  
643 (c)-(d) XRD diffractograms of a clastic sample from the last detritic interval (c) and from the  
644 last stromatolitic horizon (d) showing a superlattice reflections of 29-30 Å (red circles) that  
645 indicates a mixed layer mineral C/S MLM more enriched in smectite than chlorite in the upper  
646 part of the section. Minerals: calcite=Ca, chlorite=C, K-Feldspar=F, (I) Illite/Mica=MI, mixed  
647 layers chlorite/smectite, plagioclase=P, quartz=q.

648  
649 **Figure 9** SEM images of aggregates extracted from the spherulites. (a-g) Spherical or globular  
650 morphologies. (h,l) Irregular morphologies.

651  
652 **Figure 10** (a-b) SEM images of an example of preserved EPS sheets and joined aggregates  
653 (white arrows). (c) SEM image of globular aggregates preserving a sheet covering a portion of  
654 the aggregates (white square). (d) EDS analyses of the aggregates and the sheet reveal a silica-  
655 rich composition (green circle) containing some carbon (black circle) in the aggregates (Spot

1). The sheets contain considerable amounts of carbon relative to silica, and detectable proportions of sulfur, magnesium, chlorine and arsenic (Spot 2).

**Figure 11** (a) Details of aggregates showing coccoidal and coccobacilli-like crystals indicated by white arrows and related EDS analysis showing a predominantly silica-rich composition and some carbon. (b) Coccoidal bacterial-like molds embedded in calcite crystals indicated by white arrows. (c) Clay minerals in dark columnar stromatolitic Laminae. (d) 3D SEM photomicrograph of a 3D spherulitic samples composed primarily of radially arranged calcite crystals forming cortices and micritic circular nuclei marked by a dashed line (e=EDS analyses of nucleus showing a composition of calcite associated with clays containing Si, Al, K, and iron (Fe). (f)=EDS analysis suggests the cortices are composed mostly of pure calcite).

## 668    **References**

- 669    Adachi, N., Ezaki, Y., Liu, J., Watabe, M., Sonoda, H., Altanshagai, G., Enkhbaatar, B.  
670    Dorjnamjaa, D. (2019). Late Ediacaran Boxonia-bearing stromatolites from the Gobi-Altay,  
671    western Mongolia. *Precambrian Research*, 334, 105470.  
672    <https://doi.org/10.1016/j.precamres.2019.105470>
- 673    Altermann, W., Kazmierczak, J., Oren, A., & Wright, D. T. (2006). Cyanobacterial  
674    calcification and its rock-building potential during 3.5 billion years of Earth history.  
675    *Geobiology*, 4, 147–166. <https://doi.org/10.1111/j.1472-4669.2006.00076.x>
- 676    Álvaro, J. J., Ezzouhairi, H., Ait Ayad, N., Charif, A., Solá, R., & Ribeiro, M. L. (2010).  
677    Alkaline lake systems with stromatolitic shorelines in the Ediacaran volcanosedimentary  
678    Ouarzazate Supergroup, Anti-Atlas, Morocco. *Precambrian Research*, 179(1–4), 22–36.  
679    <https://doi.org/10.1016/j.precamres.2010.02.009>
- 680    Álvaro, J. J., & González-Acebrón, L. (2019). Sublacustrine hydrothermal seeps and  
681    silicification of microbial bioherms in the Ediacaran Oued Dar’a caldera, Anti-Atlas,  
682    Morocco. *Sedimentology*, (ii). <https://doi.org/10.1111/sed.12568>
- 683    Andres, M. S., & Pamela Reid, R. (2006). Growth morphologies of modern marine  
684    stromatolites: A case study from Highborne Cay, Bahamas. *Sedimentary Geology*, 185(3–4),  
685    319–328. <https://doi.org/10.1016/J.SEDGEO.2005.12.020>
- 686    Arp, G., Helms, G., Karlinska, K., Schumann, G., Reimer, A., Reitner, J., & Trichet, J.  
687    (2012). Photosynthesis versus Exopolymer Degradation in the Formation of Microbialites on  
688    the Atoll of Kiritimati, Republic of Kiribati, Central Pacific. *Geomicrobiology Journal*, 29(1),  
689    29–65. <https://doi.org/10.1080/01490451.2010.521436>

690 Aubineau, J., El Albani, A., Bekker, A., Somogyi, A., Bankole, O. M., Macchiarelli, R.,  
 691 Meunier, A., Riboulleau, A., Reynaud, J., Konhauser, K. O. (2019). Microbially induced  
 692 potassium enrichment in Paleoproterozoic shales and implications for reverse weathering on  
 693 early Earth. *Nature Communications*, 10(1), 2670. [https://doi.org/10.1038/s41467-019-10620-](https://doi.org/10.1038/s41467-019-10620-3)  
 694 3

695 Banerjee, S., Sarkar, S., Eriksson, P. G., & Samanta, P. (2010). Microbially Related  
 696 Structures in Siliciclastic Sediment Resembling Ediacaran Fossils: Examples from India,  
 697 Ancient and Modern. *Geobiology*, 109–129. [https://doi.org/10.1007/978-90-481-3799-2\\_6](https://doi.org/10.1007/978-90-481-3799-2_6)

698 Bosak, T., Bush, J. W. M., Flynn, M. R., Liang, B., Ono, S., Petroff, A. P., & Sim, M. S.  
 699 (2010). Formation and stability of oxygen-rich bubbles that shape photosynthetic mats.  
 700 *Geobiology*, 8(1), 45-55. <https://doi.org/10.1111/j.1472-4669.2009.00227.x>

701 Bosak, Tanja, Knoll, A. H., & Petroff, A. P. (2013). The Meaning of Stromatolites. *Annual*  
 702 *Review of Earth and Planetary Sciences*, 41(1), 21–44. [https://doi.org/10.1146/annurev-earth-](https://doi.org/10.1146/annurev-earth-042711-105327)  
 703 042711-105327

704 Bosak, Tanja, Liang, B., Min, S. S., & Petroff, A. P. (2009). Morphological record of  
 705 oxygenic photosynthesis in conical stromatolites. *Proceedings of the National Academy of*  
 706 *Sciences of the United States of America*, 106(27), 10939–10943.  
 707 <https://doi.org/10.1073/pnas.0900885106>

708 Bottjer, D., & Hagadorn, J. W. (2007). Mat growth features. *Atlas of Microbial Mat Features*  
 709 *Preserved Within the Clastic Rock Record*. Elsevier, Amsterdam, New York, 53-71. Bouton,  
 710 A., Vennin, E., Pace, A., Bourillot, R., Dupraz, C., Thomazo, C., Brayard, A., Désaubliaux,  
 711 G., Visscher, P. T. (2016). External controls on the distribution, fabrics and mineralization of  
 712 modern microbial mats in a coastal hypersaline lagoon, Cayo Coco (Cuba). *Sedimentology*,  
 713 63(4), 972–1016. <https://doi.org/10.1111/sed.12246>

714 Chagas, A. A. P., Webb, G. E., Burne, R. V., & Southam, G. (2016). Modern lacustrine  
 715 microbialites: Towards a synthesis of aqueous and carbonate geochemistry and mineralogy.  
 716 *Earth-Science Reviews*, 162, 338–363. <https://doi.org/10.1016/j.earscirev.2016.09.012>

717 Chafetz, H., Barth, J., Cook, M., Guo, X., & Zhou, J. (2018). Origins of carbonate spherulites:  
 718 implications for Brazilian Aptian pre-salt reservoir. *Sedimentary Geology*, 365, 21-33.  
 719 <https://doi.org/10.1016/j.sedgeo.2017.12.024>

720 Chi Fru, E., Arvestål, E., Callac, N., El Albani, A., Kiliyas, S., Argyraki, A., & Jakobsson, M.  
 721 (2015). Arsenic stress after the Proterozoic glaciations. *Scientific Reports*, 5, 17789.  
 722 <https://doi.org/10.1038/srep17789>

723 Chi Fru, E., Callac, N., Posth, N. R., Argyraki, A., Ling, Y. C., Ivarsson, M., Broman, C.,  
 724 Kiliyas, S. P. (2018). Arsenic and high affinity phosphate uptake gene distribution in shallow  
 725 submarine hydrothermal sediments. *Biogeochemistry*, 141(1), 41–62.  
 726 <https://doi.org/10.1007/s10533-018-0500-8>

727 Choubert, G., Faure-Muret, A. (1970). Les corrélations du Précambrien, Anti-Atlas occidental  
 728 et central. Colloque international sur les corrélations du Précambrien: Agadir – Rabat, 3–23  
 729 mai 1970. Livret guide de l’excursion : Anti-Atlas occidental et central. *Notes et Mémoires*  
 730 *Du Service Géologique Du Maroc*, 229, 259.

731 Dongjie, T., Xiaoying, S., Ganqing, J., Yunpeng, P., Wenhao, Z., Yuan, W., & Min, L.  
 732 (2013). Environment controls on Mesoproterozoic thrombolite morphogenesis: A case study  
 733 from the North China Platform. *Journal of Palaeogeography*, 2(3), 275–296.

734 Dupraz, C., & Visscher, P. T. (2005). Microbial lithification in marine stromatolites and  
 735 hypersaline mats. *Trends in Microbiology*, 13(9), 429–438.  
 736 <https://doi.org/10.1016/J.TIM.2005.07.008>

737 Eymard, I., Alvarez, M. del P., Bilmes, A., Vasconcelos, C., & Ariztegui, D. (2020). Tracking  
 738 Organomineralization Processes from Living Microbial Mats to Fossil Microbialites.  
 739 Minerals, 10(7), 605. <https://doi.org/10.3390/min10070605>  
 740 Gerdes, G. (2010). What are Microbial Mats? [https://doi.org/10.1007/978-90-481-3799-2\\_1](https://doi.org/10.1007/978-90-481-3799-2_1)  
 741 Gerdes, G., Klenke, T., & Noffke, N. (2000). Microbial signatures in peritidal siliciclastic  
 742 sediments: A catalogue. *Sedimentology*, 47(2), 279–308. [https://doi.org/10.1046/j.1365-](https://doi.org/10.1046/j.1365-3091.2000.00284.x)  
 743 3091.2000.00284.x  
 744 Harwood, C. L., & Sumner, D. Y. (2011). Microbialites of the Neoproterozoic Beck Spring  
 745 Dolomite, Southern California. *Sedimentology*, 58(6), 1648–1673.  
 746 <https://doi.org/10.1111/j.1365-3091.2011.01228.x>  
 747 Hickman-Lewis, K., Cavalazzi, B., Foucher, F., & Westall, F. (2018). Most ancient evidence  
 748 for life in the Barberton greenstone belt: Microbial mats and biofabrics of the ~3.47 Ga  
 749 Middle Marker horizon. *Precambrian Research*, 312, 45–67.  
 750 <https://doi.org/10.1016/j.precamres.2018.04.007>  
 751 Kaźmierczak, J., Kempe, S., Kremer, B., López-García, P., Moreira, D., & Tavera, R. (2011).  
 752 Hydrochemistry and microbialites of the alkaline crater lake Alchichica, Mexico. *Facies*,  
 753 57(4), 543–570. <https://doi.org/10.1007/s10347-010-0255-8>  
 754 Kirkham, A., & Tucker, M. E. (2018). Thrombolites, spherulites and fibrous crusts  
 755 (Holkerian, Purbeckian, Aptian): Context, fabrics and origins. *Sedimentary Geology*, 374, 69–  
 756 84. <https://doi.org/10.1016/j.sedgeo.2018.07.002>  
 757 Knoll, A. H., Bergmann, K. D., & Strauss, J. V. (2016,). Life: The first two billion years.  
 758 Philosophical Transactions of the Royal Society B: *Biological Sciences*, Vol. 371 (1707),  
 759 20150493. <https://doi.org/10.1098/rstb.2015.0493>



760 Kremer, B., Kaźmierczak, J., & Kempe, S. (2019). Authigenic replacement of  
 761 cyanobacterially precipitated calcium carbonate by aluminium-silicates in giant microbialites  
 762 of Lake Van (Turkey). *Sedimentology*, 66(1), 285–304. <https://doi.org/10.1111/sed.12529>  
 763 Kulp, T. R., Hoeft, S. E., Asao, M., Madigan, M. T., Hollibaugh, J. T., Fisher, J. C., Stolz, J.  
 764 F., Culbertson, C. W., Miller, L. G., Oremland, R. S. (2008). Arsenic(III) fuels anoxygenic  
 765 photosynthesis in hot spring biofilms from Mono Lake, California. *Science*, 321(5891), 967–  
 766 970. <https://doi.org/10.1126/science.1160799>  
 767 McCann Hoeft, S., Boren, A., Hernandez-Maldonado, J., Stoneburner, B., Saltikov, C., Stolz,  
 768 J., & Oremland, R. (2016). Arsenite as an Electron Donor for Anoxygenic Photosynthesis:  
 769 Description of Three Strains of Ectothiorhodospira from Mono Lake, California and Big Soda  
 770 Lake, Nevada. *Life*, 7(1), 1. <https://doi.org/10.3390/life7010001>  
 771 Mercedes-Martín, R., Rogerson, M. R., Brasier, A. T., Vonhof, H. B., Prior, T. J., Fellows, S.  
 772 M., Reijmer, J.J.G. Billing, I. Pedley, H. M. (2016). Growing spherulitic calcite grains in  
 773 saline, hyperalkaline lakes: experimental evaluation of the effects of Mg-clays and organic  
 774 acids. *Sedimentary Geology*, 335, 93–102. 335, 93–102.  
 775 <https://doi.org/10.1016/J.SEDGEO.2016.02.008>  
 776 Merino, N., Aronson, H. S., Bojanova, D. P., Feyhl-Buska, J., Wong, M. L., Zhang, S., &  
 777 Giovannelli, D. (2019). Living at the extremes: Extremophiles and the limits of life in a  
 778 planetary context. *Frontiers in Microbiology*, 10, 780.  
 779 <https://doi.org/10.3389/fmicb.2019.00780>  
 780 Monty, C. L. V. (1976). The Origin and Development of Cryptalgal Fabrics. *Developments in*  
 781 *Sedimentology*, 20, 193–249. [https://doi.org/10.1016/S0070-4571\(08\)71137-3](https://doi.org/10.1016/S0070-4571(08)71137-3)

782 Moore, D. M., & Reynolds Jr, R. C. (1989). X-ray Diffraction and the Identification and  
 783 Analysis of Clay Minerals. Oxford University Press (OUP).

784 Noffke, N., & Awramik, S. M. (2013). Stromatolites and MISS-Differences between relatives.  
 785 GSA Today, 23(9), 4–9. <https://doi.org/10.1130/GSATG187A.1>

786 Pecoraino, G., & Alessandro, W. D. (2015). The Other Side of the Coin: Geochemistry of  
 787 Alkaline Lakes in Volcanic Areas. *Volcanic lakes*, 219-237. [https://doi.org/10.1007/978-3-](https://doi.org/10.1007/978-3-642-36833-2)  
 788 642-36833-2

789 Perri, E., Tucker, M. E., Słowakiewicz, M., Whitaker, F., Bowen, L., & Perrotta, I. D. (2018).  
 790 Carbonate and silicate biomineralization in a hypersaline microbial mat (Mesaieed sabkha,  
 791 Qatar): Roles of bacteria, extracellular polymeric substances and viruses. *Sedimentology*,  
 792 65(4), 1213–1245. <https://doi.org/10.1111/sed.12419>

793 Planavsky, N., & Grey, K. (2008). Stromatolite branching in the Neoproterozoic of the  
 794 Centralian Superbasin, Australia: an investigation into sedimentary and microbial control of  
 795 stromatolite morphology. *Geobiology*, 6(1), 33-45. [https://doi.org/10.1111/j.1472-](https://doi.org/10.1111/j.1472-4669.2007.00116.x)  
 796 4669.2007.00116.x

797 Reid, R. P., James, N. P., Macintyre, I. G., Dupraz, C. P., & Burne, R. V. (2003). Shark Bay  
 798 stromatolites: Microfabrics and reinterpretation of origins. *Facies*, 49(1), 299.  
 799 <https://doi.org/10.1007/s10347-003-0036-8>

800 Riding, R. (1991). Classification of Microbial Carbonates. *Calcareous Algae and*  
 801 *Stromatolites*. 21–51. [https://doi.org/10.1007/978-3-642-52335-9\\_2](https://doi.org/10.1007/978-3-642-52335-9_2)

802 Riding, R. (2011). Microbialites, stromatolites, and thrombolites. *Encyclopedia of geobiology*.  
 803 <https://doi.org/10.1007/978-1-4020-9212-1>

804 Sallstedt, T., Bengtson, S., Broman, C., Crill, P. M., & Canfield, D. E. (2018). Evidence of  
805 oxygenic phototrophy in ancient phosphatic stromatolites from the Paleoproterozoic  
806 Vindhyan and Aravalli Supergroups, India. *Geobiology*, 16(2), 139–159.  
807 <https://doi.org/10.1111/gbi.12274>

808 Sancho-Tomás, M., Somogyi, A., Medjoubi, K., Bergamaschi, A., Visscher, P.T., Van  
809 Driessche A.E.S., Gérard, E., Farias, M.E., Contreras, M., Philippot, P. (2018). Distribution,  
810 redox state and (bio)geochemical implications of arsenic in present day microbialites of  
811 Laguna Brava, Salar de Atacama. *Chemical. Geology*. 490, 13–21.  
812 <https://doi.org/10.1016/j.chemgeo.2018.04.029>

813 Sanz-Montero, M. E., Cabestrero, Ó., & Sánchez-Román, M. (2019). Microbial Mg-rich  
814 Carbonates in an Extreme Alkaline Lake (Las Eras, Central Spain). *Frontiers in*  
815 *Microbiology*, 10, 148. <https://doi.org/10.3389/fmicb.2019.00148>

816 Schagerl, M., & Burian, A. (2016). The ecology of African soda lakes: driven by variable and  
817 extreme conditions. *Soda Lakes of East Africa*. 12, 295–320. [https://doi.org/10.1007/978-3-](https://doi.org/10.1007/978-3-319-28622-8)  
818 [319-28622-8](https://doi.org/10.1007/978-3-319-28622-8)

819 Sforza, M.C., Daye, M., Philippot, P., Somogyi, A., van Zuilen, M.A., Medjoubi, K., Gérard, E.,  
820 Jamme, F., Dupraz, C., Braissant, O., Glunk, C., & Visscher, P.T. (2017). Patterns of metal  
821 distribution in hypersaline microbialites during early diagenesis: implications for the fossil  
822 record. *Geobiology*, 15(2), 259–279. <https://doi.org/10.1111/gbi.12218>

823 Sforza, M. C., Philippot, P., Somogyi, A., Van Zuilen, M. A., Medjoubi, K., Schoepp-Cothenet,  
824 B., Nitshke, W., Visscher, P. T. (2014). Evidence for arsenic metabolism and cycling by  
825 microorganisms 2.7 billion years ago. *Nature Geoscience*, 7, 811–815.  
826 <https://doi.org/10.1038/ngeo2276>

827 Sheng, G.-P., Yu, H.-Q., & Li, X.-Y. (2010). Extracellular polymeric substances (EPS) of  
 828 microbial aggregates in biological wastewater treatment systems: A review. *Biotechnology*  
 829 *Advances*, 28(6), 882–894. <https://doi.org/10.1016/J.BIOTECHADV.2010.08.001>

830 Skilling, I. P., White, J. D. L., & McPhie, J. (2002). Peperites: A review of magma-sediment  
 831 mingling. *Journal of Volcanology and Geothermal Research*, 114(1–2), 1–17.  
 832 [https://doi.org/10.1016/S0377-0273\(01\)00278-5](https://doi.org/10.1016/S0377-0273(01)00278-5)

833 Środoń, J. (1999). Nature of Mixed-Layer Clays and Mechanisms of Their Formation and  
 834 Alteration. *Annual Review of Earth and Planetary Sciences*, 27(1), 19–53.  
 835 <https://doi.org/10.1146/annurev.earth.27.1.19>

836 Stüeken, Eva E., & Buick, R. (2018). Environmental control on microbial diversification and  
 837 methane production in the Mesoarchean. *Precambrian Research*, 304, 64–72.  
 838 <https://doi.org/10.1016/j.precamres.2017.11.003>

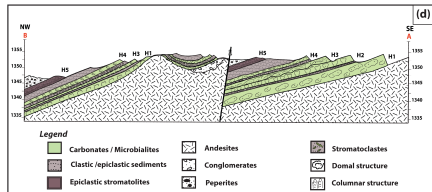
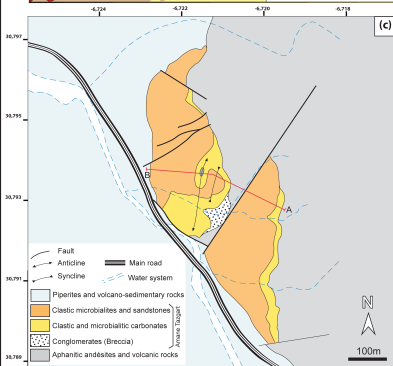
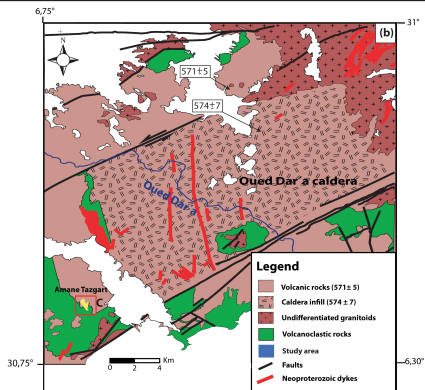
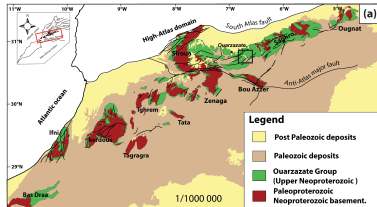
839 Suarez-Gonzalez, P., Benito, M. I., Quijada, I. E., Mas, R., & Campos-Soto, S. (2019).  
 840 ‘Trapping and binding’: A review of the factors controlling the development of fossil  
 841 agglutinated microbialites and their distribution in space and time. *Earth-Science Reviews*,  
 842 194, 182–215. <https://doi.org/10.1016/j.earscirev.2019.05.007>

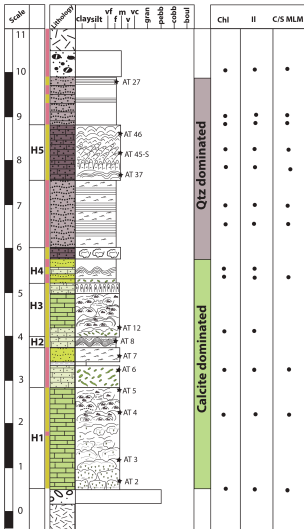
843 Sumner, D. Y., Hawes, I., Mackey, T. J., Jungblut, A. D., & Doran, P. T. (2015). Antarctic  
 844 microbial mats: A modern analog for Archean lacustrine oxygen oases. *Geology*, 43(10), 887–  
 845 890. <https://doi.org/10.1130/G36966.1>

846 Tang, D., Shi, X., & Jiang, G. (2013). Mesoproterozoic biogenic thrombolites from the North  
 847 China platform. *International Journal of Earth Sciences*, 102(2), 401–413.  
 848 <https://doi.org/10.1007/s00531-012-0817-9>

849 Thomas, R. J., Chevallier, L. P., Gresse, P. G., Harmer, R. E., Eglington, B. M., Armstrong,  
 850 R. A., De Beer, C. H., Martini, J. E. J., De Kock, G. S., Macey, P. H., Ingram, B. A. (2002).  
 851 Precambrian evolution of the Sirwa Window, Anti-Atlas Orogen, Morocco. *Precambrian*  
 852 *Research*, 118(1–2), 1–57. [https://doi.org/10.1016/S0301-9268\(02\)00075-X](https://doi.org/10.1016/S0301-9268(02)00075-X)  
 853 Thomas, R. J., Fekkak, A., Ennih, N., Errami, E., & Loughlin, S. C. (2004). A new  
 854 lithostratigraphic framework for the Anti-Atlas Orogen, Morocco. *Journal of African Earth*  
 855 *Sciences*, 39(3-5), 217-226. <https://doi.org/10.1016/j.jafrearsci.2004.07.046>  
 856 Tuduri, J., Chauvet, A., Barbanson, L., Bourdier, J., Labriki, M., Ennaciri, A., Badra, L.,  
 857 Dubois, M., Ennaciri-leloix, C., Sizaret, S., Maacha, L. (2018). The Jbel Saghro Au (– Ag ,  
 858 Cu ) and Ag – Hg Metallogenetic Province : Product of a Long-Lived Ediacaran Tectono-  
 859 Magmatic Evolution in the Moroccan Anti-Atlas. *Minerals*, 8(12), 592.  
 860 <https://doi.org/10.3390/min8120592>  
 861 Van Kranendonk, M. J., Djokic, T., Poole, G., Tadbiri, S., Steller, L., & Baumgartner, R.  
 862 (2019). Depositional Setting of the Fossiliferous, c.3480 Ma Dresser Formation, Pilbara  
 863 Craton. *Earth's Oldest Rocks*, 985–1006. [https://doi.org/10.1016/b978-0-444-63901-](https://doi.org/10.1016/b978-0-444-63901-1.00040-x)  
 864 [1.00040-x](https://doi.org/10.1016/b978-0-444-63901-1.00040-x)  
 865 Walsh, G. J., Benziane, F., Aleinikoff, J. N., Harrison, R. W., Yazidi, A., Burton, W. C.,  
 866 Quick, J. E., Saadane, A. (2012). Neoproterozoic tectonic evolution of the Jebel Saghro and  
 867 Bou Azzer—El Graara inliers, eastern and central Anti-Atlas, Morocco. *Precambrian*  
 868 *Research*, 216–219, 23–62. <https://doi.org/10.1016/J.PRECAMRES.2012.06.010>  
 869 Willmer, P., Stone, G., & Johnston, I. (2004). *Environmental Physiology of Animals* (2nd  
 870 ed.).

- 871 Wright, V. P., & Barnett, A. J. (2015). An abiotic model for the development of textures in  
872 some South Atlantic early Cretaceous lacustrine carbonates. *Geological Society Special*  
873 *Publication*, 418(1), 209–219. <https://doi.org/10.1144/SP418.3>
- 874 Xiao, M., Li, M., & Reynolds, C. S. (2018). Colony formation in the cyanobacterium  
875 *Microcystis*. *Biological Reviews*, 93(3), 1399–1420. <https://doi.org/10.1111/brv.12401>












## Legende


### Facies

-  Carbonate
-  Sandy limestones
-  Calcarenitic
-  Sandstones
-  Clastic stromatolites
-  Silty sands
-  Conglomerates
-  Peperites
-  Andesites
-  Microbialite-derived clasts

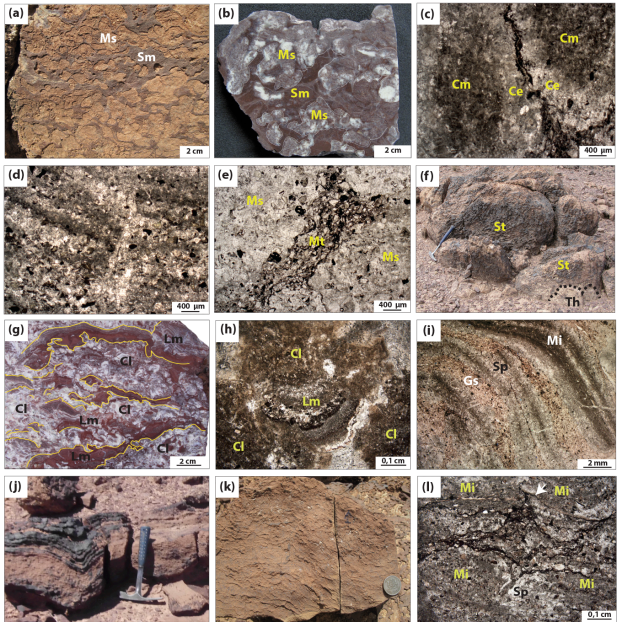
### Sedimentary structures

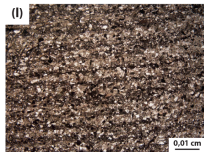
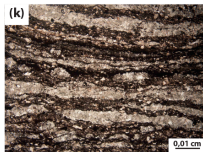
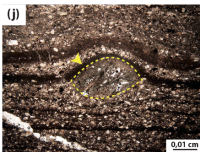
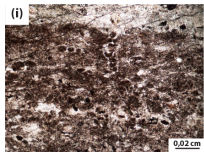
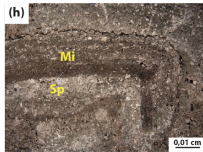
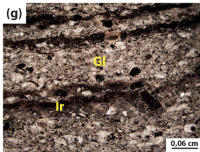
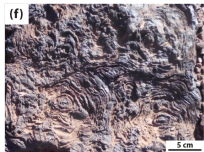
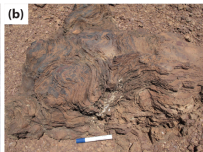
-  Ripple bedding
-  Planar laminated
-  Composite microbialites
-  Domal structure
-  Flat domal stromatolites
-  Columnar stromatolites
-  Spherulites

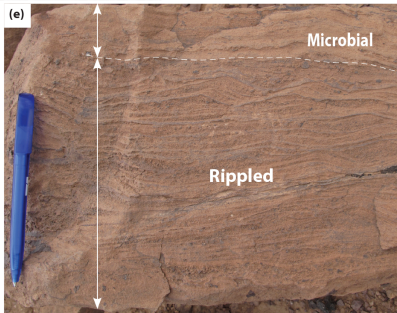
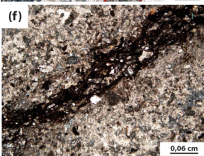
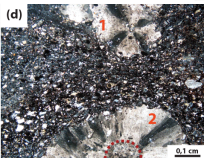
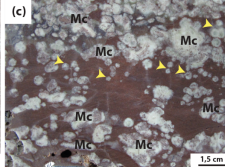
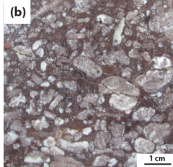
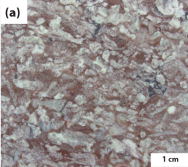
### Facies type

-  Microbial origin
-  Physical origin

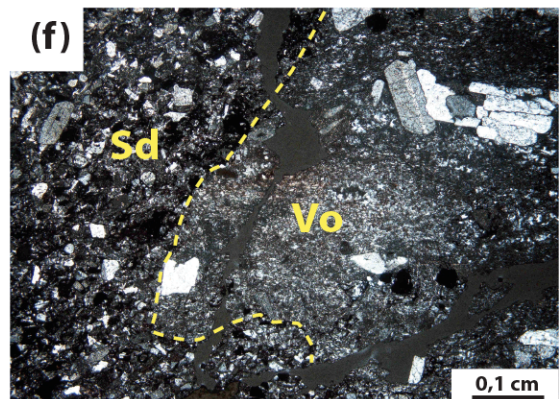
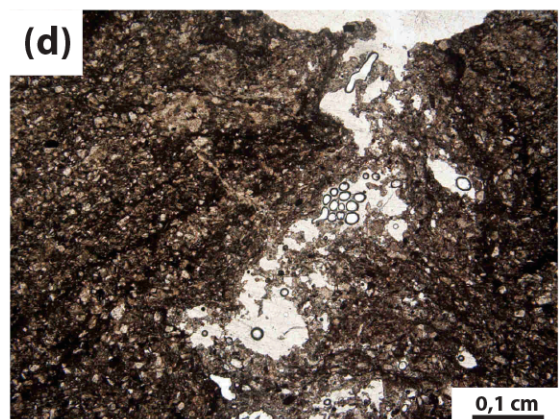
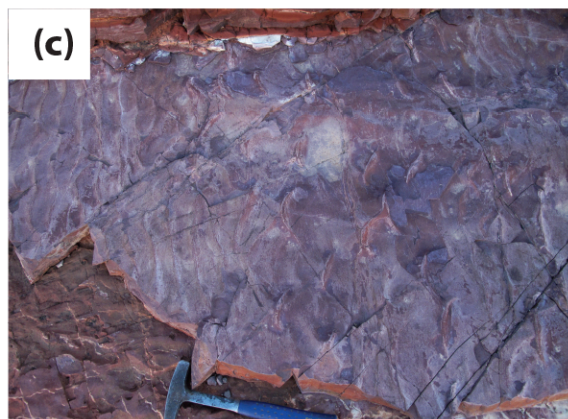




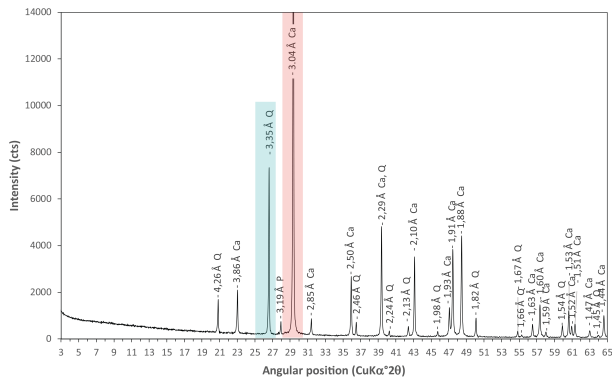




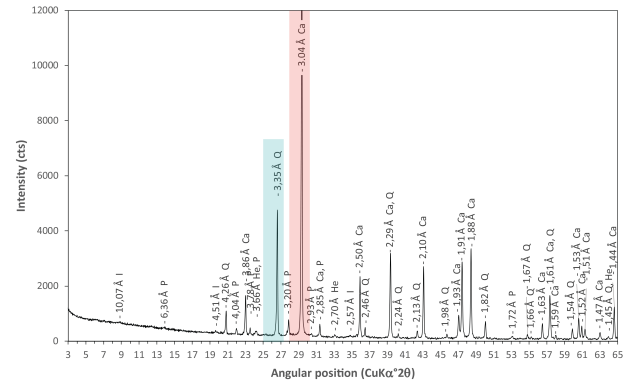




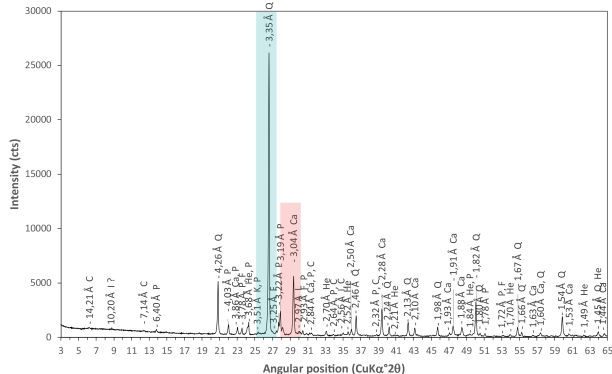
(a)



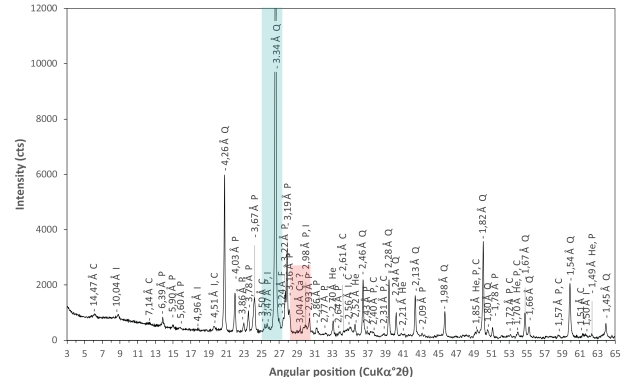
(b)



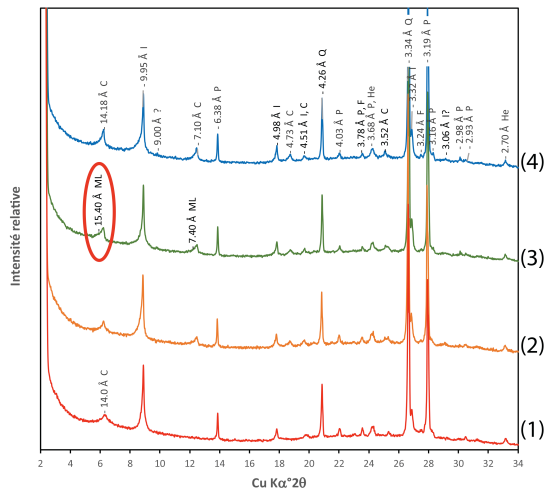
(c)



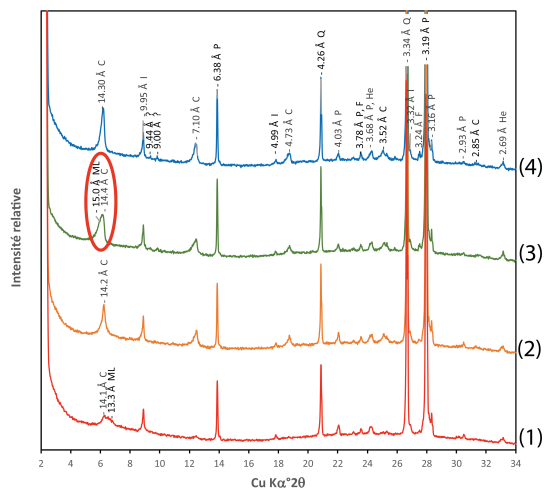
(d)



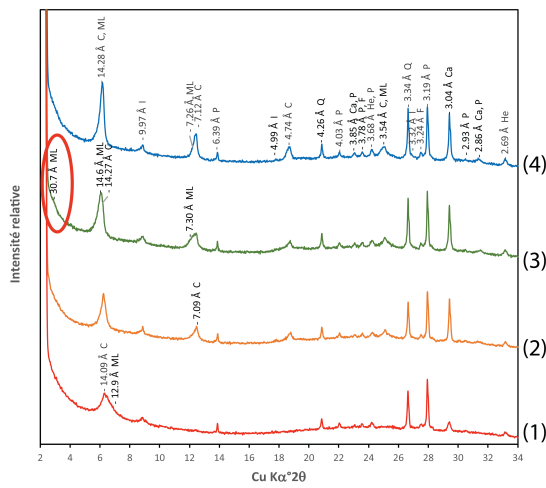
(a)



(b)



(c)



(d)

